Nano Research

Open Access

Research Article

A multi-affinity supramolecular nanolayer reinforced PVDF-LLZTO composite polymer electrolyte for stable solid-state lithium batteries

Changfei Liu, Sailong Wang, Zhengyi Lu, Jiaqing Zhao, Yuchen Wu, Chaojie Ren, Ruizhi Yang ✉, and Chao Jin ✉

College of Energy, Soochow Institute for Energy and Materials Innovations, Soochow University, Suzhou 215006, China

Cite this article: *Nano Research*, **2025**, *18*, 94907087. https://doi.org/10.26599/NR.2025.94907087

ABSTRACT: Technical breakthrough of composite polymer electrolyte (CPE) is one of the key factors that determines the commercial process of the current solid-state lithium battery. However, high interface impedance limits its electrochemical performances. It is crucial to optimize the design of multiphase interfaces among different components in CPE for regulating Li^+ transport. Herein, a multi-affinity self-assembled 12-crown-4-TFSI (12C4-TFSI) supramolecular nanolayer is introduced into poly(vinylidene difluoride)-$Li_{6.75}La_3Zr_{1.75}Ta_{0.25}O_{12}$ (PVDF-LLZTO) CPE as interface modifier. As a result, enhanced Li^+ conductivity of 4.29 × 10^{-4} S·cm^{-1}, Li^+ transfer number of 0.44, and stable electrochemical window voltage of 4.8 V vs. Li/Li^+ at 30 °C are obtained. The symmetric Li||Li cell exhibits an improved critical current density (CCD) of 1.2 mA·cm^{-2} and steady cycling at 0.2 mA·cm^{-2} for over 850 h without visible voltage fluctuation. The assembled Li||$LiFePO_4$ coin solid-state cell delivers a high initial discharge capacity of 172.9 mAh·g^{-1} at 0.1 C, rate capability (up to 5.0 C) and outstanding cycling stability with a capacity retention of 87.2% after over 750 cycles at 1.0 C. The associated Li||$LiFePO_4$ pouch cell presents an initial specific discharge capacity of 112.3 mAh·g^{-1} and successfully runs 30 cycles with a final capacity of 101.8 mAh·g^{-1}. This work offers a facile strategy to optimize multiphase interfaces of PVDF-LLZTO CPE for stable solid-state lithium battery.

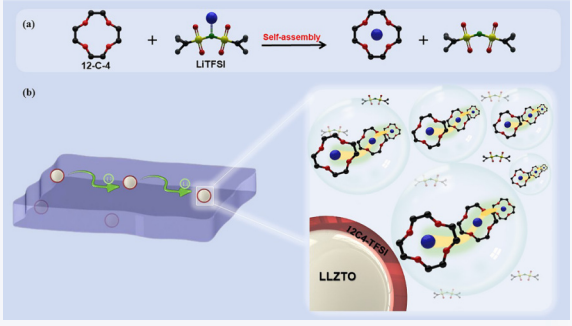

KEYWORDS: solid-state lithium battery, composite polymer electrolyte, interface impedance, modifier, supramolecular

1 Introduction

Since high energy density, inspiring safety, and fast charging/discharging capability, solid state lithium batteries (SSLBs) have been attracting widespread attention to meet the rapid development of electric vehicles [1]. As a key component of SSLBs, solid state electrolytes (SSEs) still face lots of challenges, including poor electrical properties, unacceptable stability, uncontrollable SSE/electrode solid–solid interface [2, 3]. In order to well undress these concerns, various SSEs have been developed and reported. Generally, there are three types SSEs, inorganic solid electrolytes (ISEs), solid polymer electrolytes (SPEs), and composite polymer electrolytes (CPEs). Each SSE has its own unique advantages, such as relatively high ionic conductivity [4] and excellent tolerance against lithium dendritic growth for the ISEs [5], good interfacial compatibility with electrodes, high flexibility and processing friendly mechanical property for the SPEs [6–8]. While, CPEs combine these merits, which are considered as the most promising SSEs closing to commercial application at present [9].

Typically, CPEs are composed of three components: polymer matrix, inorganic filler, and lithium salt. A lot types of CPEs, including polyethylene oxide (PEO)-$Li_{6.75}La_3Zr_{1.75}Ta_{0.25}O_{12}$ (LLZTO)-bis(trifluoromethane)sulfonimide lithium salt (LiTFSI), PEO-$Li_{1.3}Al_{0.3}Ti_{1.7}(PO_4)_3$(LATP)-LiTFSI, polyether sulfone (PESF)-LLZTO-LiTFSI, polyvinylidene fluoride (PVDF)-LLZTO-$LiClO_4$, and polytetrafluoroethylene (PTFE)-LLZTO-succinonitrile (SN) [10–14], have been well studied. Among them, PEO-based CPEs have been thoroughly researched, however, some intrinsic weaknesses, such as poor ionic conductivity, a limited electrochemical window, and inadequate thermal stability, limit their practical application [15]. In comparison, PVDF-LLZTO based CPEs have been attracting much attention due to relatively high ionic conductivity and Li^+ transference number, a wide electrochemical window and desirable electrochemical stability. Although significant achievements have been obtained in PVDF-LLZTO based CPEs, some unaddressed scientific and technological

Received: August 30, 2024; **Revised:** October 17, 2024
Accepted: October 18, 2024

✉Address correspondence to Ruizhi Yang, yangrz@suda.edu.cn; Chao Jin, jinchao@suda.edu.cn

issues should be continuously concerned before their commercialization. First of all, owing to the huge surface energy difference between PVDF and LLZTO, it is difficult to get uniform dispersion of active LLZTO fillers in PVDF matrix, spontaneous agglomeration of LLZTO particles will be adverse to Li^+ transport, leading to inferior conductivity [16, 17]. Secondly, LLZTO is sensitive to water and CO_2 in the air, an Li_2CO_3 passive layer will be generated on the LLZTO particle surface when exposed in a trace moisture environment [18, 19], which worsens the compatibility between fillers and polymer matrix. Moreover, the rigid nature of both PVDF skeleton and LLZTO ceramic will incur inadequate interfacial contacts between different components in CPEs, and even CPEs/electrode interfaces, which usually results in enormous polarization resistance [20, 21]. Therefore, more efforts should be involved to optimize interfacial compatibility in PVDF-LLZTO based CPEs.

Various approaches have been put forward to solve above-mentioned issues. For example, Wu and co-workers successfully achieved F^- anions partially substituting for the O^{2-} ions in the LLZTO grains and Al_2O_3/AlF_3 meliorating the grain boundaries to suppress the formation of Li_2CO_3 and improve lithiophilicity of LLZTO [19]. Kuhnert et al. screened the oxygen polarity of LLZTO particles via a plasma-etching process, which obviously reduced interfacial resistance of CPEs [22]. In addition, modification/grafting of functional polymers nanolayer on the surface of active fillers has been verified to be an effective strategy to optimize interfacial contact among different components in CPEs. Wu and his collaborators successfully introduced a dual-functional modification layer (defined as LATP@SCA-0.25IL) onto the surface of LATP particles by employing silane coupling agent (SCA) and ionic liquid (IL), utilizing chemical grafting and ion exchange strategies [23]. He et al. modified the surface of LLZTO with a silane coupling agent, which improved even distribution and promoted the Li^+ migration [24]. Besides, some organic small molecule, such as maleic acid [25], itaconic acid [11], stearic acid [26], dopamine [27], and β-cyclodextrin [10], can be also used as functional surface modifier to optimize interfacial compatibility of CPEs. Recently, crown ethers are well known due to their excellent selectivity to chelate various alkali metal cations. Each type crown ether owns its distinctive ring-like cavity structure, which is capable of accommodating alkali metal ions with different ionic radiuses [28]. In especial, 12-crown-4 (12C4) has a cavity radius (0.072–0.081 nm) close to that of Li^+, which is very suitable for capturing Li^+ [29].

Inspired by those scenarios, in this work, 12C4 supramolecular with self-assembled LiTFSI salt (12C4-TFSI) is introduced as a "multi-affinity" surface modifier to enhance compatibility of PVDF-LLZTO based CPEs, as depicted in Scheme 1. Briefly, 12C4-TFSI is well bound to LLZTO through hydrogen bonding to produce a uniformly protective nanolayer [30], which can not only avoid the formation of inert Li_2CO_3, reduce the surface energy of LLZTO, and then improve the interface compatibility between LLZTO fillers and PVDF matrix, but more importantly, can promote the dissociation of LiTFSI, increase the active Li^+ in LLZTO, and provide a high-speed Li^+ diffusion channel via a host–guest interaction. As a result, the as-derived PVDF-LLZTO@12C4-TFSI CPE delivers a Li^+ conductivity of 4.29×10^{-4} S·cm^{-1} at 30 °C, an enhanced Li^+ transfer number of 0.44. The as-assembled SSLBs based on $LiFePO_4$ cathode successfully run over 750 cycles at 1.0 C and 30 °C.

2 Experimental

2.1 Materials

LLZTO powders were purchased from Prof. Xiangxin Guo's group. PVDF (HSV900) was purchased from MTI chemicals. Conductive agent (Super P), LiTFSI (99.9%, DoDoChem), and commercial $LiFePO_4$ (LFP) powders were dried at 80 °C for 24 h under vacuum before used. Supramolecular 12C4 was bought from J&K Scientific.

The self-assembled 12C4-TFSI was prepared as follows: 0.5 g LiTFSI and 0.307 g 12C4 were firstly added into 20 mL deionized water, and stirred for 12 h at room temperature (RT), then treated by a 24-h lyophilization process. The final obtained powder was labelled as 12C4-TFSI. The yield was ~ 95%.

Fabrication of LLZTO@12C4-TFSI: The as-prepared 12C4-TFSI was dissolved in 10 mL N, N-dimethylformamide (DMF), then 2.0 g LLZTO powder was added and magnetically stirred in a glove box for 12 h. After that, the 12C4-TFSI surface modified LLZTO was centrifuged and dried in a vacuum oven at 60 °C for 36 h, then finally denoted as LLZTO@12C4-TFSI. For comparisons, different LLZTO@12C4-TFSI samples with different modifier thicknesses were prepared by controlling relative weight percent of 12C4-TFSI with LLZTO powders (3%, 5%, and 10%), and named as LLZTO@12C4-TFSI-x (x = 3, 5, and 10), respectively. Here, we should note that the final LLZTO@12C4-TFSI-5 was also designated as LLZTO@12C4-TFSI.

2.2 Preparation of PVDF-LLZTO@12C4-TFSI CPEs

PVDF-LLZTO@12C4-TFSI CPEs were fabricated and controlled via a traditional tap-casting process. PVDF and LiTFSI (3:1 weight ratio) were firstly dissolved in DMF and stirred at 50 °C for 6 h to obtain a homogeneous solution with a PVDF concentration of 10 wt.%. Then, the as-prepared LLZTO@12C4-TFSI powders were added into the solution and stirred with a weight ratio of 10 wt.% of the total amount of PVDF and LLZTO. Subsequently, the

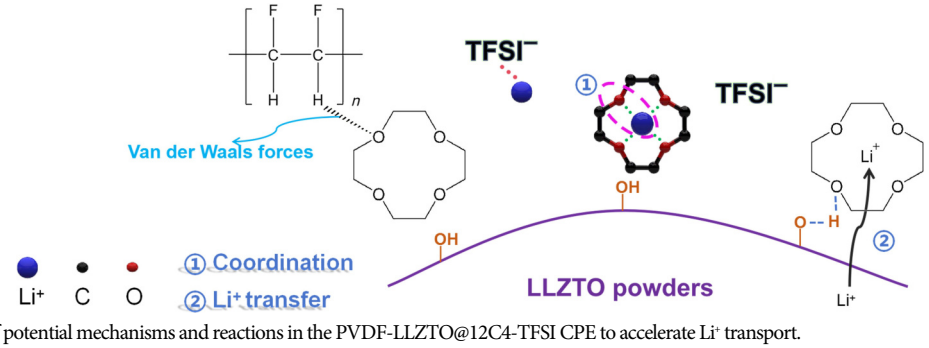

Scheme 1 Illustration of potential mechanisms and reactions in the PVDF-LLZTO@12C4-TFSI CPE to accelerate Li^+ transport.

homogeneous slurry was casted on a clean PTFE sheet to obtain green PVDF-LLZTO@12C4-TFSI CPEs. After dried in a vacuum oven at 60 and 120 °C for 24 h to thoroughly remove trace solvent, the final PVDF-LLZTO@12C4-TFSI CPEs were obtained. According to the same process, the PVDF-LLZTO CPEs, PVDF-LLZTO@12C4-TFSI-*x* CPEs were also prepared, respectively.

2.3 Characterization

X-ray diffraction (XRD) was performed using a Bruker D8 Advance equipment with Cu Kα radiation from 10° to 80° to probe the crystal structure of the materials. Scanning electron microscopy (SEM, Hitachi SU8010) and transmission electron microscopy (TEM, FEI Tecnai-G2 F20 operating at 200 kV) were employed to visualize the morphology of samples. X-ray photoelectron spectroscopy (XPS) was carried out on Thermo Fisher Escalab 250Xi with the Al Ka line as the excitation source to study the surface chemical compositions of sample. Thermogravimetric analysis (TGA) was performed on TG/DTA7300 (SII NanoTechnology) at a heating rate of 10 °C·min^{-1} from 20 to 800 °C in static air. ^{1}H NMR spectra were recorded at 400 MHz with a AVANCENEO NMR spectrometer at 25 °C. Differential scanning calorimetry (DSC) measurements were performed on a Mettler-Toledo STAR system from −50 to 220 °C. Fourier transform infrared spectroscopy (FTIR) spectra were carried out on a TENSOR 27 equipment (Bruker Optics, Germany). Contact angles of both the pristine LLZTO and the LLZTO@12C4-TFSI-5 on 10 wt.% PVDF solution were measured on a contact angle instrument (JGW-360DZ). Solid state NMR spectra were obtained by Bruker 600M at the Qingdao Institute of Bioenergy and Bioprocess Technology.

2.4 Electrochemical test

CR2032 coin-type symmetric cells of SS‖CPEs‖SS (stainless steel) were assembled and measured by electrochemical impedance spectroscopy (EIS) to evaluate Li^+ conductivity of the as-prepared CPEs at different temperatures. EIS was tested on an Autolab PGStat302N electrochemical workstation with an AC amplitude of 10 mV in a frequency range of 1.0 MHz to 0.1 Hz. The ionic conductivity (σ) can be calculated according to Eq. (1)

$$\sigma = l/RS \quad (1)$$

where l is thickness (cm) of the CPEs, R is the measured resistance (Ω), S is the effective contact area (cm^2) between CPEs and SS electrode.

CR2032 coin-type symmetric cells of Li‖CPEs‖Li were used to assess the Li^+ transference number (t_{Li^+}) of the as-prepared CPEs via direct current (DC) polarization with EIS characterizations. t_{Li^+} can be calculated according to Eq. (2) [31]

$$t_{Li^+} = I_{SS}(\Delta V - I_0R_0)/I_0(\Delta V - I_{SS}R_{SS}) \quad (2)$$

where I_0 is the initial current, I_{SS} is the steady state current, ΔV is the direct current polarization voltage with a value of 10 mV applied to the Li‖CPEs‖Li symmetrical cells. R_0 is the initial charge-transfer resistance and R_{SS} is the steady-state charge-transfer resistance of the CSEs.

Li‖CPEs‖Li symmetric cells were also used to estimate electrochemical interfacial compatibility and stability between CPEs and Li metal anode through galvanostatic charge–discharge cycling measurements with different current densities (0.05–1.2 mA·cm^{-2}) and a fixed 2 h for each cycle at 30 °C on LAND CT2001A testing system.

CR2032 coin-type half cells of Li‖CPEs‖SS were measured to characterize the stable electrochemical window voltage (SEWV) of the as-prepared CPEs via linear sweep voltammetry (LSV) test from open circuit voltage (OCV) to 6.0 V at a scanning rate of 10 mV·s^{-1} at 30 °C.

Both CR2032-coin type and pouch type Li‖CPEs‖$LiFePO_4$ SSLBs were assembled and measured to explore the practical application of the optimized PVDF-LLZTO@12C4-TFSI CPEs. The thickness of CPEs was ~ 70 μm, and the $LiFePO_4$ loading was ~ 1.7 mg·cm^{-2}. The size of the pouch cell was 5 cm × 5 cm with a thickness of ~ 1 mm. The charge–discharge performance and cycling stability were measured on a LAND CT 2001A testing system within a voltage range of 2.5 to 4.0 V (vs. Li^+/Li) at 30 °C.

3 Results and discussion

Figure S1(a) in the Electronic Supplementary Material (ESM) shows molecular structures related to 12C4 and LiTFSI. 12C4 is a macrocyclic oligoether containing polar ligand functional groups, its cavity diameter is well-suited for complexation with Li^+ [28]. Therefore, 12C4 can effectively promote the dissociation of lithium salts via a host–guest interaction between crown ether and LiTFSI. ^{1}H NMR, ^{6}Li NMR, FTIR, and XRD characterizations were carried out to confirm this host–guest interaction, as exhibited in Figs. S1(b)–S1(e) in the ESM, respectively. Compared with the fresh 12C4, ^{1}H NMR results show that a positive chemical shift in 12C4-TFSI can be observed, indicating the change of the electron cloud density within the cavity due to the entry of Li^+ [32]. ^{6}Li NMR results of LiTFSI and 12C4-TFSI further verified the supramolecular interaction between 12C4 and LiTFSI. As for FTIR, the asymmetric stretching vibrational absorption peak of both CF_3 and S–N–S coming from LiTFSI, and C–O–C bending vibration coming from 12C4 still exist in the 12C4-TFSI, except for a slight negative shift. In addition, XRD characteristic peaks of LiTFSI are clearly visible in the 12C4-TFSI. All above mentioned results suggest that LiTFSI can be successfully self-assembled into the cavity of 12C4 to generate a supramolecular combination, and the process did not destroy the molecular structures of both 12C4 and LiTFSI. After a facile wet chemical treatment, LLZTO particles were successfully surface coated by the as-prepared 12C4-TFSI supramolecular assemblies. As presented in Fig. 1(a), XRD results suggest that 12C4-TFSI surface modification layer shows excellent chemical compatibility with LLZTO, these characteristic peaks of the LLZTO@12C4-TFSI continue to closely match the standard cubic LLZO garnet phase (JCPDS 80-0457). The F 1s high-resolution XPS spectrum (Fig. 1(b)) shows that a new strong peak (~ 688.5 eV) associated with $-CF_3$ appears in the LLZTO@12C4-TFSI [33], which originates from the $TFSI^-$ part of the 12C4-TFSI supramolecular assembly. The peak (~ 685 eV) related with the Li–F bond is primarily attributed to the pristine LLZTO. Compared with that in the pristine LLZTO, the Li–F peak in the LLZTO@12C4-TFSI shows a negative shift due to a synergy effect of both a self-existent Li–F in the 12C4-TFSI supramolecular nanolayer and a strong coordination between the cavity of 12C4 with Li^+ on the surface LLZTO. The C 1s high-resolution XPS spectrum (Fig. S2 in The ESM) indicates that 12C4-TFSI surface modification can effectively avoid the generation of Li_2CO_3 due to the greatly weakened peak associated with Li_2CO_3 in the

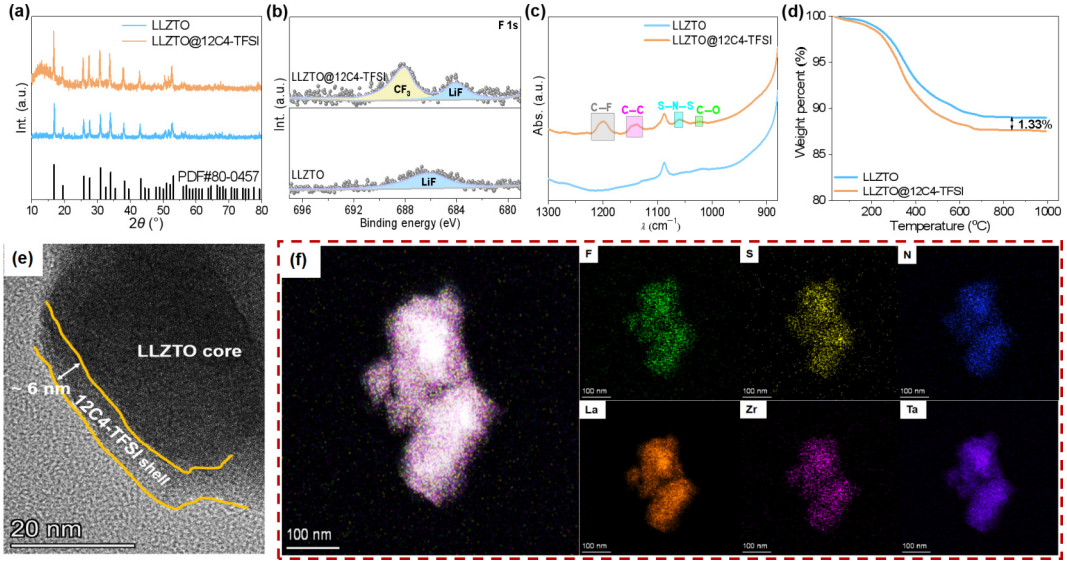

Figure 1 Physical characterizations of the pristine LLZTO and the as-prepared LLZTO@12C4-TFSI powders: (a) XRD patterns, (b) F 1s high-resolution XPS spectrum, (c) FTIR, (d) TG curves, (e) and (f) TEM image and related element mapping images of EDS of the LLZTO@12C4-TFSI, respectively.

LLZTO@12C4-TFSI. FTIR spectra are displayed in Fig. 1(c). Compared with that of the pristine LLZTO, some additional absorption peaks are present in the LLZTO@12C4-TFSI, including a C–O peak (~ 1022 cm^{-1}) and a C–C peak (~ 1140 cm^{-1}) coming from the 12C4, as well as a C–F characteristic peak at ~ 1200 cm^{-1} and an S–N–S characteristic peak at ~ 1060 cm^{-1} originating from the self-assembled LiTFSI [10, 34]. These observations further confirm the presence of the 12C4-TFSI surface modification layer on the LLZTO particles. TG analysis (Fig. 1(d)) shows that the content of 12C4-TFSI is ~ 1.33 wt.% on the surface of the LLZTO. To visually display the presence of the coating layer, Figs. 1(e) and 1(f) present high-resolution TEM (HRTEM) image of the LLZTO@12C4-TFSI and related element mapping images of energy dispersive spectroscopy (EDS), respectively. A clear core–shell structure can be observed with LLZTO as core and 12C4-TFSI as shell with a thickness of ~ 6 nm, and the 12C4-TFSI shell is homogeneously distributed in LLZTO particles. Line energy dispersive X-ray analysis (EDAX) result further proved the presence of the core–shell structure (Fig. S3 in the ESM). Strong hydrogen bonding promotes the formation of the continuous and tight interfacial contact between the LLZTO core and the 12C4-TFSI shell.

Uniform dispersibility of ceramic fillers in polymer solution is a key factor that must be considered during the CPE fabricating/drying process [35]. Since the big difference in surface energy between LLZTO and PVDF/DMF solution, there tends to be the LLZTO aggregation phenomenon, which will be adverse to conductivity and mechanical strength of the as-prepared CPEs. Figures 2(a) and 2(b) display the contact angle of 10 wt.% PVDF in DFM solution droplets on the surface of both the LLZTO wafer and

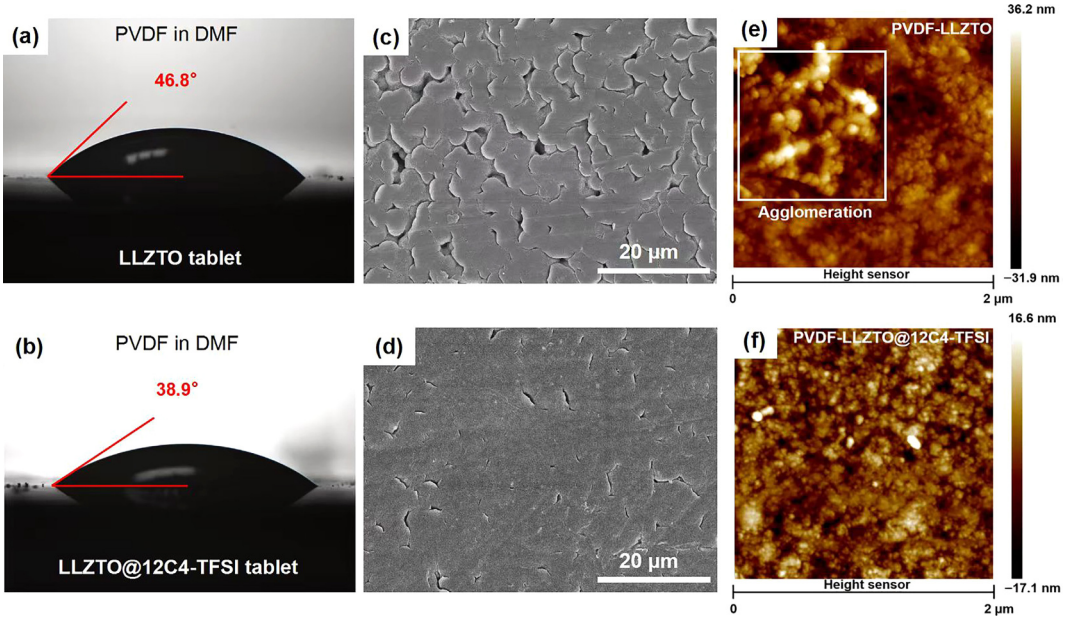

Figure 2 (a) and (b) Contact angles between 10 wt.% PVDF in DMF solutionand fresh LLZTO or LLZTO@12C4-TFSI, respectively. (c) and (d) Surface SEM images and (e) and (f) surface AFM images of both the PVDF-LLZTO CPE and the PVDF-LLZTO@12C4-TFSI CPE.

the LLZTO@12C4-TFSI wafer, respectively. After the surface modification, the contact angle reduced from 46.8° to 38.9°, suggesting that the 12C4-TFSI nanolayer helps to lower surface energy of LLZTO nanoparticles. The sedimentation experiment also confirmed the result (Fig. S4 in the ESM). Figures 2(c) and 2(d) present surface SEM images of the as-prepared PVDF-LLZTO CPE and PVDF-LLZTO@12C4-TFSI CPE, respectively. Obviously, the latter exhibits a more smooth and denser surface, the enhanced dispersibility of LLZTO particles in PVDF matrix contributes to the result. Atomic force microscopy (AFM) images in the surface view of two CPEs, as shown in Figs. 2(e) and 2(f), further verified the optimized LLZTO nanoparticles distribution in the PVDF-LLZTO@12C4-TFSI CPE. In addition, Fig. S5 in the ESM shows the cross-sectional SEM images of both CPEs. Visible LLZTO particles aggregation with a size of ~ 5 μm can be observed in the PVDF-LLZTO CPE. All characterizations indicate that the 12C4-TFSI surface modification can effectively reduce surface energy difference and optimize LLZTO nanoparticles distribution. Benefitting from the optimized microstructure, a flexible PVDF-LLZTO@12C4-TFSI CPE in meter level with controllable thickness and micromorphology can be easily fabricated in lab. Normally, PVDF undergoes dehydrofluorination side reaction in an alkaline-like environment, which will bring a noticeable color change to dark brown in PVDF-based CPEs [36, 37]. Besides, previous studies suggested that La atoms in LLZTO are prone to react with DMF, resulting in structural damage of garnet [38]. And there is a dehydrofluorination reaction in PVDF-LLZTO family. These two side reactions will bring a noticeable color change [13]. Unlike the common dark brown of the PVDF-LLZTO CPE, the as-prepared PVDF-LLZTO@12C4-TFSI CPE shows a white color similar to LLZTO nanoparticles (Fig. S6 in the ESM), further confirming that the 12C4-TFSI surface modification can not only effectively inhibit Li_2CO_3 and LiOH contamination on the LLZTO surface, but also mitigate above-mentioned dehydrofluorination side reaction to stabilize PVDF matrix.

SS‖CPEs‖SS symmetric cells were assembled and measured to investigate the impact of 12C4-TFSI nanolayer on the ionic conductivity of the PVDF-LLZTO CPEs. Figure S7 in the ESM presents EIS plots of the PVDF-LLZTO CPE and PVDF-LLZTO@12C4-TFSI-x (x = 3 wt.%, 5 wt.%, and 10 wt.%) CPEs at a temperature range of 0–60 °C. According to Eq. (1), the corresponding Li^+ conductivities (σ_{Li^+}) are calculated and summarized in Table S1 in the ESM. Compared with the PVDF-LLZTO CPE, it can be observed that all CPEs with 12C4-TFSI modified nanolayer exhibited improved conductivity at each testing temperature. Especially, the PVDF-LLZTO@12C4-TFSI-5 CPE delivered the highest ionic conductivity of 4.29×10^{-4} S·cm^{-1} at 30 °C and 6.85×10^{-4} S·cm^{-1} at 60 °C, which were over 1.5 times than that of the PVDF-LLZTO CPE (2.71×10^{-4} S·cm^{-1} at 30 °C and 4.21×10^{-4} S·cm^{-1} at 60 °C). As for values of σ_{Li^+}, the as-prepared PVDF-LLZTO@12C4-TFSI-5 CPE is similar to/even better than some previously reported PVDF-LLZTO based CPEs [13, 39–44]. Moreover, it can be also seen that too much 12C4-TFSI is actually detrimental to conductivity, for example, the PVDF-LLZTO@12C4-TFSI-10 CPE shows a decreased σ_{Li^+} from 2.99×10^{-4} S·cm^{-1} (x = 3) and 4.29×10^{-4} S·cm^{-1} (x = 5) to 2.73×10^{-4} S·cm^{-1} at 30 °C. Actually, 12C4-TFSI supramolecular nanolayer in this work acts as a bridge to closely connect PVDE matrix, LLZTO filler, and LITFSI salt, and a multi-affinity modifier to optimize interface contact among these components in CPE. If the dosage of the 12C4-TFSI is too small, it will not guarantee sufficient connection and then affect the synergistic effect; if the dosage is too much, it will increase the thickness of nanolayer, and then affect Li^+ transport to a certain extent. Figure 3(a) illustrates Arrhenius plots for these CPEs. The PVDF-LLZTO@12C4-TFSI-5 CPE delivers a lower active energy (E_a) of 0.1117 eV than the PVDF-LLZTO CPE does (0.1134 eV), suggesting that more channels were probably involved in Li^+ transmission.

Figures 3(b) and 3(c) illustrate DC polarization curves and corresponding initial and steady-state EIS spectra for the PVDF-LLZTO CPE and the PVDF-LLZTO@12C4-TFSI-5 CPE, respectively. Lithium-ion transfer number (t_{Li^+}) increased from 0.27 for the PVDF-LLZTO CPE to 0.44 for the PVDF-LLZTO@12C4-TFSI-5 CPE. This can be ascribed to more free Li^+ ions in PVDF matrix after introducing 12C4-TFSI, which weakened interaction between Li^+ and $TFSI^-$ anion through competitive coordination [45].

Figure 3(d) shows LSV plots of these CPEs measured by Li‖CPEs‖SS half cells at 30 °C. The SEWV was expanded partly after 12C4-TFSI modification, improved from ~ 4.6 V for the PVDF-LLZTO to ~ 4.8 V for the PVDF-LLZTO@12C4-TFSI-5. This improved SEWV is hypothesized to a more uniform charge distribution, thereby minimizing charge concentration difference in local areas [46].

Figures 3(e) and 3(f) demonstrate polarization curves of the Li‖CPEs‖Li symmetric cells at different conditions to estimate electrochemical compatibility and stability against Li dendrites during Li plating/stripping process. As shown in Fig. 3(e), the PVDF-LLZTO CPE tends to create short circuit even at a critical current densities (CCD) of 0.5 mA·cm^{-2}, which is in agreement with Ref. [20]. While, the short circuit phenomenon only occurred when the CCD reached 1.2 mA·cm^{-2} for the PVDF-LLZTO@12C4-TFSI-5 CPE. Figure 3(f) shows that the PVDF-LLZTO CPE just ran ~ 300 h with a polarization overpotential exceeding 90 mV at 0.2 mA·cm^{-2} then a short circuit happened. In contrast, the PVDF-LLZTO@12C4-TFSI-5 CPE exhibited a smaller polarization overpotential of 70 mV and successfully cycled for over 850 h without significant voltage fluctuation. Even, the excellent stability is better than some reported PVDF-based CPEs (Table S2 in the ESM). Moreover, surface characterizations (digital photo, SEM, and AFM images) of Li metal anode before and after Li plating/stripping under different statuses (operating at different CCDs), as presented in Fig. S8 in the ESM, further prove that the as-prepared PVDF-LLZTO@12C4-TFSI-5 CPE can preferably restrict lithium dendrites. Figure 3(g) compares four key characteristics (σ_{Li^+}, SEWV, t_{Li^+}, and CCD) of the as-prepared PVDF-LLZTO@12C4-TFSI-5 CPE and previously reported PVDF-LLZO based CPEs. It is noticeable that property of this work is relatively more balanced.

In order to further understand the Li compatibility difference of two CPEs, Figs. 4(a) and 4(b) present their Nyquist plots of Li‖CPEs‖Li symmetric cells measured at different stages at 0.2 mA·cm^{-2} and fixed 0.2 mAh·cm^{-2}, respectively. Compared with the fresh status, both cells exhibited a great impedance decrease after the first cycling, which is associated with the formation of a solid electrolyte interface (SEI) [47]. After that, a relatively stable impedance at different stages was obtained for the PVDF-LLZTO@12C4-TFSI-5 CPE based cell, which is similar with its polarization behaviors shown in Fig. 3(f). However, the PVDF-LLZTO CPE based cell demonstrated a continuously decreasing impedance, one of explanations is the gradual formation of undesired Li dendrite and/or pulverization. After their respective Li

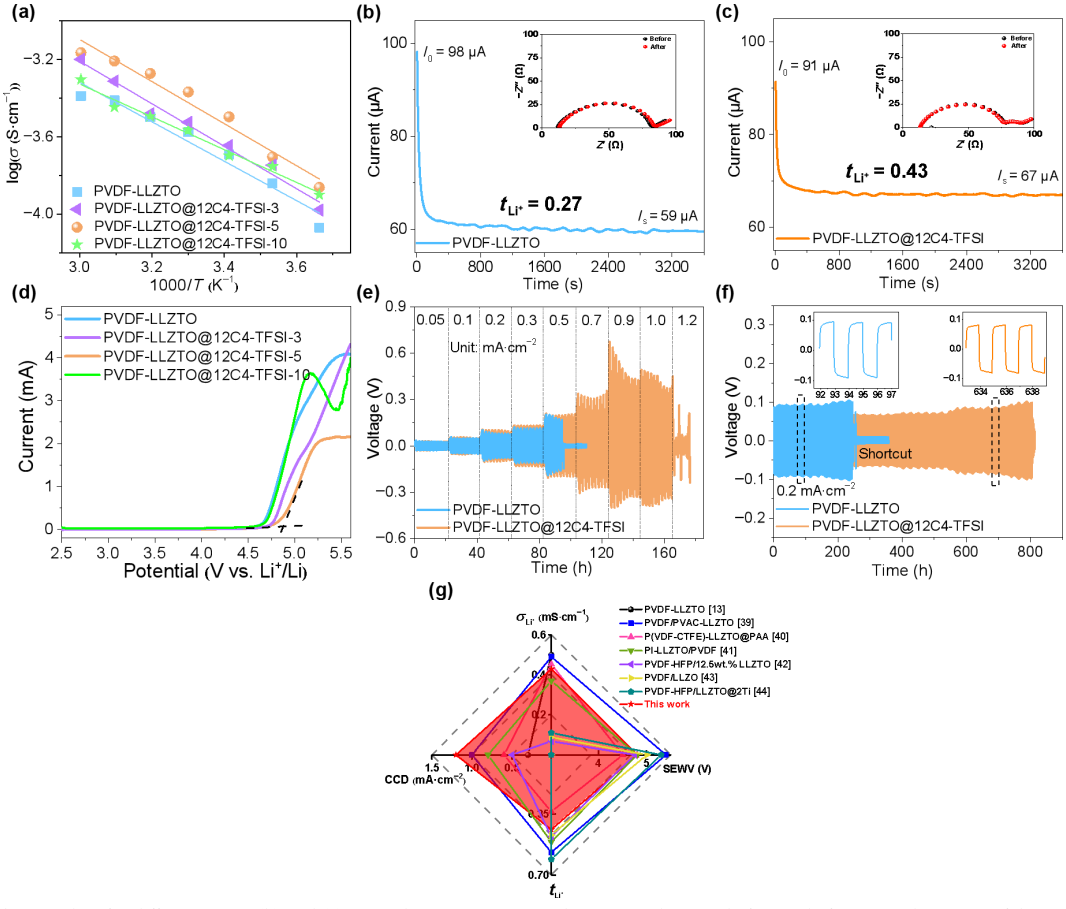

Figure 3 (a) Arrhenius plots for different CPEs. (b) and (c) DC polarization curves and corresponding EIS before and after DC polarization of the PVDF-LLZTO CPE and the PVDF-LLZTO@12C4-TFSI CPE, respectively. (d) LSV plots of different CPEs measured by Li‖CPEs‖SS half cells at 30 °C. Polarization curves of the Li‖CPEs‖Li symmetric cells at different conditions: (e) rate performance and (f) long-term stability, respectively. (g) Radar chart of four key parameters.

plating/stripping cycling died, both cells were disassembled and analyzed to study morphological changes in both Li and CPEs. Figures 4(c) and 4(d) display surface SEM images of Li anode, respectively. It can be clearly observed that the Li anode surface close to the PVDF-LLZTO CPE exhibits severe pulverization (Fig. 4(c)), while that near the PVDF-LLZTO@12C4-TFSI-5 CPE is relatively integrated and smooth (Fig. 4(d)). Surface SEM images of both CPEs close to Li anode were also characterized, as shown in Figs. 4(e) and 4(f), respectively. Similarly, the PVDF-LLZTO@12C4-TFSI-5 CPE presents a relatively flat and clean surface (Fig. 4(f)). These results indicate that the PVDF-LLZTO@12C4-TFSI-5 CPE can provide a more stable and compatible interface with Li metal anode. It is known that positively charged oxygen vacancies can serve as Lewis acid sites with strong affinity for the $TFSI^-$ anions, which helps to promote the dissociation of LiTFSI salts to release more free Li^+ ions [48–50]. Moreover, the presence of oxygen vacancy can induce a local electric field due to the lopsided charge distribution, which will facilitate the detachment of Li^+ near oxygen vacancies from the LLZTO lattice and participate in charge transfer according to the climbing image nudged elastic band (CI-NEB) calculation [51]. To gain insight into outstanding electrochemical properties of the as-prepared PVDF-LLZTO@12C4-TFSI-5 CPE, electron paramagnetic resonance (EPR) spectroscopy was firstly carried out to reveal oxygen vacancy change between bare LLZTO and as-prepared LLZTO@12C4-TFSI particles. Figure 5(a) shows that the LLZTO@12C4-TFSI demonstrated a more intense symmetrical EPR signal at g = 2.002, indicating more oxygen vacancies [52]. The O 1s high-resolution XPS spectrum further verified the result. As exhibited in Fig. S9 in the ESM, the relative content of O_{II} associated with oxygen vacancy increased from 63% for the bare LLZTO to 73% for the as-prepared LLZTO@12C4-TFSI. It is believed that more oxygen vacancies derive from the strong coordination ability of distinctive cavity of 12C4 for Li^+, which results in outward more stable and compatible interface with Li metal anode.

As what reported in previous Refs. [53, 54], the disruption of crystallinity and expansion of amorphous region of polymer matrix benefit the rapid migration of Li^+ in CPEs. Figure 5(b) presents the DSC results of the PVDF-LLZTO CPE and the PVDF-LLZTO@12C4-TFSI-5 CPE. Both CPEs exhibited a clear endothermic peak around 150–180 °C, associated with the melting point (T_m) of PVDF matrix with varying crystallinity [55, 56]. The T_m drops from 172 °C for the PVDF-LLZTO CPE to 170 °C for the PVDF-LLZTO@12C4-TFSI-5 CPE, accordingly, the melting enthalpy value decreases from 36.3 to 29.7 $J \cdot g^{-1}$, and the calculated crystallinity of PVDF is also reduced from 34.6% to 28.3% [56], suggesting lower crystallinity and higher segment mobility of PVDF in the PVDF-LLZTO@12C4-TFSI-5 CPE.

In our previous work [57], density functional theory (DFT) calculations suggested that assembled crown ether molecules are adsorbed preferentially above Li^+ ions in LLZO(001) surface due to relatively bigger binding energy. To well understand effects of 12C4-TFSI modifier nanolayer on lithium ion occupancy of LLZTO, high-

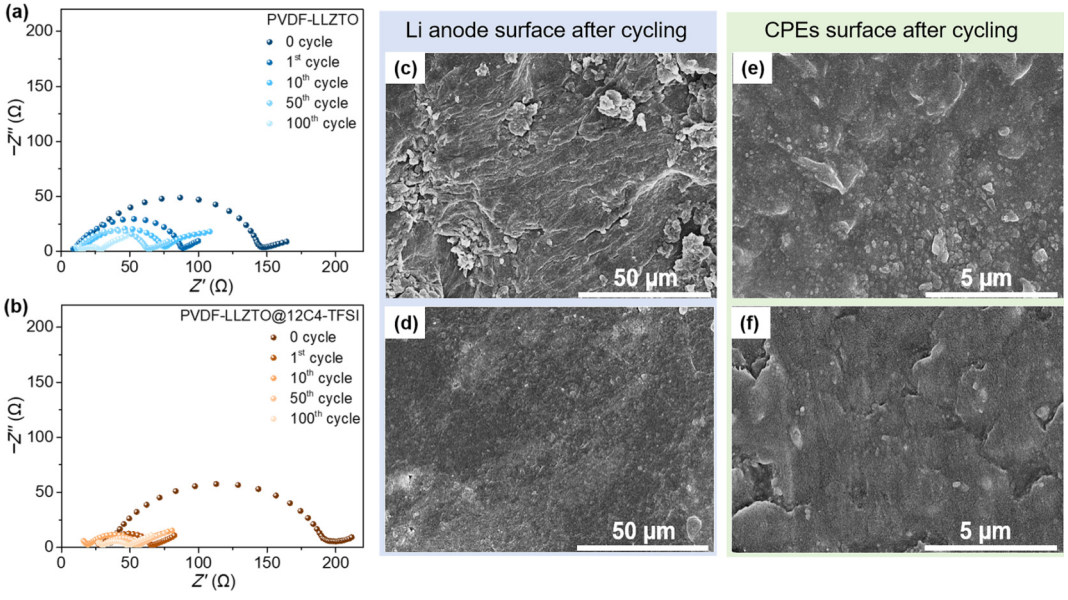

Figure 4 EIS of both Li‖CPEs‖Li symmetric cells measured at different stages: (a) PVDF-LLZTO CPE and (b) PVDF-LLZTO@12C4-TFSI-5 CPE. Surface SEM images of Li anode after cycling: (c) close to the PVDF-LLZTO CPE and (d) near the PVDF-LLZTO@12C4-TFSI-5 CPE. Surface SEM images of CPE near Li anode after cycling: (e) the PVDF-LLZTO CPE and (f) the PVDF-LLZTO@12C4-TFSI-5 CPE.

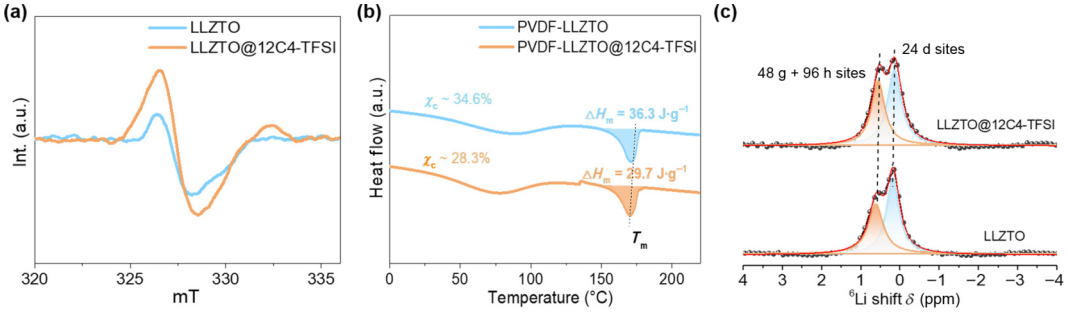

Figure 5 (a) EPR spectra of both bare LLZTO and LLZTO@12C4-TFSI powders. (b) DSC curves of both the PVDF-LLZTO CPE and the PVDF-LLZTO@12C4-TFSI-5 CPE. (c) ^{6}Li NMR spectra of pristine LLZTO and LLZTO@12C4-TFSI powders.

resolution ^{6}Li solid-state NMR spectra of both the bare LLZTO and the as-prepared LLZTO@12C4-TFSI powders have been characterized. As presented in Fig. 5(c), there appeared two obvious resonance peaks at ~ 0.55 and ~ 0.15 ppm, which can be ascribed to 48 g + 96 h sites and 24 d sites of cubic LLZO, respectively [58, 59].

Moreover, there are two critical information we should note. i) the ^{6}Li solid-state NMR peak associated with 48 g + 96 h sites is narrowed along with a slight negative shifting from 0.607 ppm in the LLZTO to 0.529 ppm in the LLZTO@12C4-TFSI, while the peak associated with 24 d sites relatively stable; ii) after integral calculations, relative peak area of 48 g + 96 h sites increased from 42% in the LLZTO to 44% in the LLZTO@12C4-TFSI. Wullen reported that lithium ions in octahedra (48 g + 96 h sites) of cubic LLZO have higher mobility than those in tetrahedra whiclh is more conducive to Li^{+} conductivity [60]. Wang and co-workers found that Li^{+} in octahedra owns higher diffusion coefficient (~ 10^{-9} $cm^{2}·s^{-1}$) than those in tetrahedra (~ 10^{-11} $cm^{2}·s^{-1}$) [61]. Therefore, we believed that the introduced 12C4-TFSI modified nanolayer contributes to reinforcing the Li^{+} migration in 48 g + 96 h sites in the LLZTO@12C4-TFSI. Figure 6(a) shows initial charge–discharge plots of CR2032-coin type Li‖CPEs‖$LiFePO_4$ SSLBs measured at 0.1 C and 30 °C. Although there appears a similar Coulombic efficiency of approximately 96%, the PVDF-LLZTO@12C4-TFSI CPE based cell delivered a higher specific discharge capacity of 172.9 $mAh·g^{-1}$ than the PVDF-LLZTO CPE based cell did (164.2 $mAh·g^{-1}$). Moreover, as depicted in Fig. 6(b), an enhanced rate capability was also achieved for the PVDF-LLZTO@12C4-TFSI CPE based SSLBs, for examples, the specific discharge capacity was 149.5, 90.9, and 147.5 $mAh·g^{-1}$ at rates of 1.0, 5.0 C and recovered 1.0 C, while, the values were only 131.6, 63.3, and 133.5 $mAh·g^{-1}$ at the same rates for the PVDF-LLZTO CPE based SSLBs, respectively. Figures 6(c) and 6(d) display long-term charge–discharge stabilities of both SSLBs measured at 0.2, 1.0 C and 30 °C, respectively. It is clearly shown that the PVDF-LLZTO@12C4-TFSI CPE based SSLBs demonstrated greatly improved stabilities, the SSLBs successfully ran over 200 cycles with a capacity retention of 84.1% at 0.2 C and over 750 cycles with a capacity retention of 87.2% at 1.0 C, respectively. Table S3 in the ESM shows electrochemical performance comparisons of different SSLBs based on PVDF-based CPEs, it can be also concluded that the as-assembled SSLBs in this work own ultrahigh cycling stability at high rate (1.0 C). Moreover, SSLBs with higher LFP loadings and NCM523 cathode are also assembled and measured, as presented in Figs. S10 and S11 in the ESM, respectively. These results further verified the antioxidant activity and the better cycling stability of the

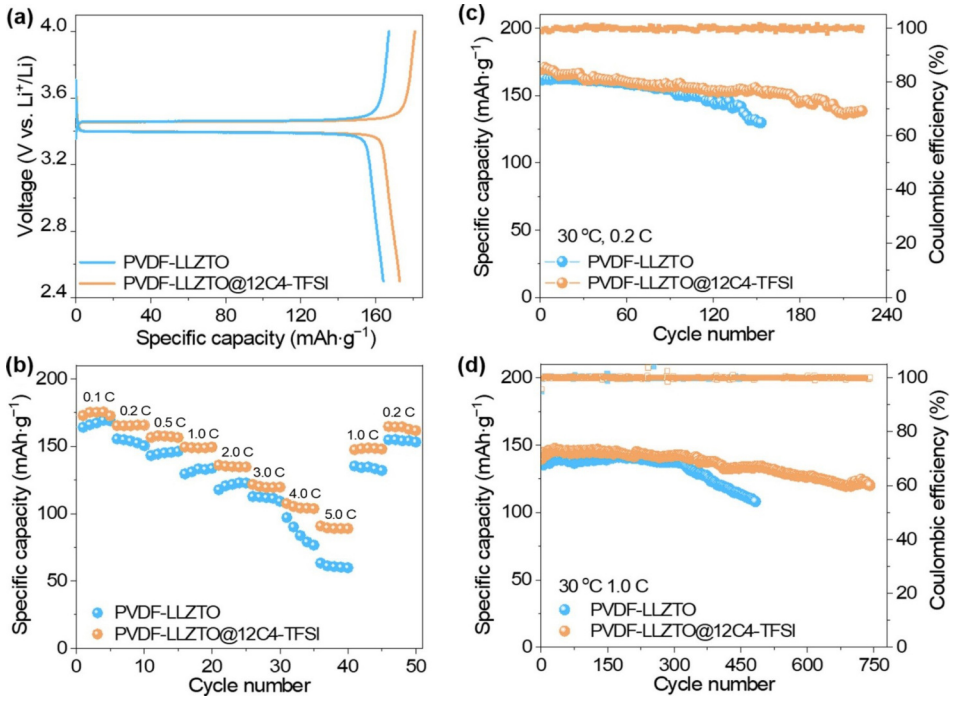

Figure 6 (a) Initial charge–discharge plots of CR2032-coin type Li|CPEs|$LiFePO_4$ SSLBs. (b) Rate capabilities; long-term charge–discharge cycling stabilities at different current densities and 30 °C: (c) 0.2 C and (d) 1.0 C, respectively.

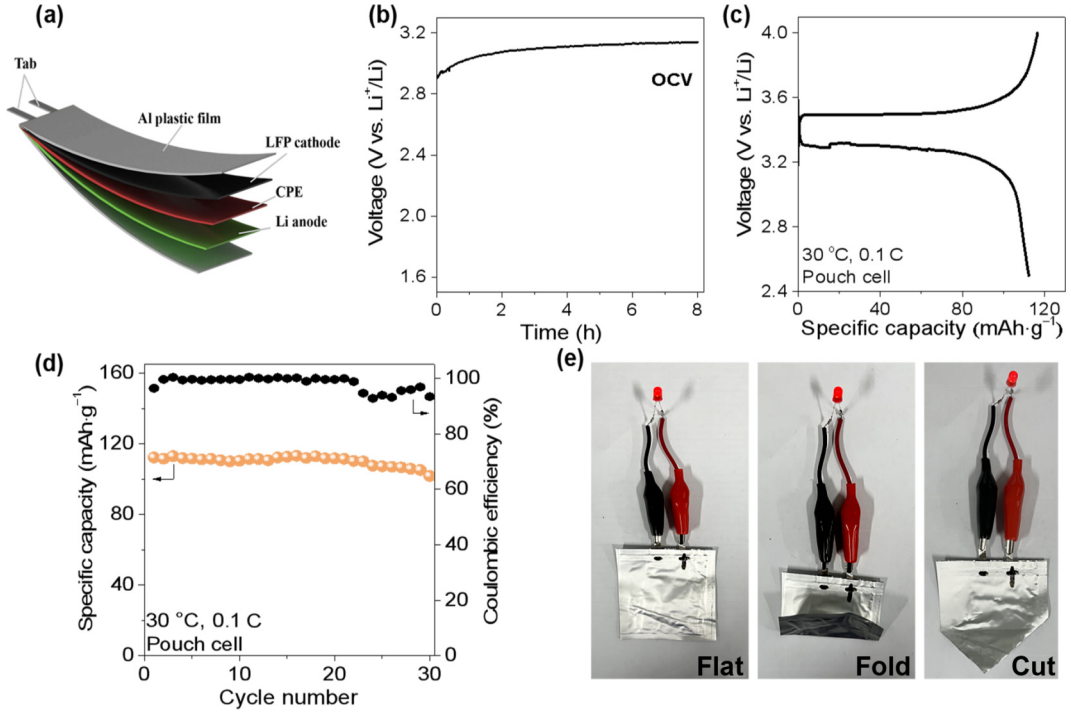

Figure 7 (a) Illustration of Li‖PVDF-LLZTO@12C4-TFSI CPE‖$LiFePO_4$ pouch cell. (b) Open circuit voltage, (c) initial charge–discharge plots, (d) charge–discharge cycling stability, and (e) photographs of the pouch cell lighting LED lamps at different conditions.

as-prepared PVDF-LLZTO@12C4-TFSI-5 CPE under high voltage from a practical application perspective.

As illustrated in Fig. 7(a), Li‖PVDF-LLZTO@12C4-TFSI CPE‖$LiFePO_4$ pouch cell with a size of 5 cm × 5 cm was assembled and tested to explore its practical application. A stable open circuit voltage close to 3.2 V was obtained (Fig. 7(b)), and an initial specific discharge capacity of 112.3 mAh·g^{-1} with a Coulombic efficiency of 96.4% was achieved (Fig. 7(c)). In addition, the pouch cell successfully operated 30 cycles with a final capacity of 101.8 mAh·g^{-1}, as shown in Fig. 7(d). Additionally, it is noteworthy that the light-emitting device (LED) lamp can be lighted under flatting, folding, and cutting conditions without short-circuit, as presented in Fig. 7(e), demonstrating excellent flexibility and potential for practical utilization.

4 Conclusions

In summary, a self-assembled 12C4-TFSI supramolecular nanolayer is coated on the surface of LLZTO fillers as multi-affinity interface modifier to adjust interface impedance of the PVDF-LLZTO CPE. Through various functions, the 12C4-TFSI supramolecular nanolayer tightly connects three parts of PVDF matrix, LLZTO filler, and LiTFSI salt, and establishes an efficient Li^+ transport network. The optimized PVDF-LLZTO@12C4-TFSI-5 CPE shows an improved σ_{Li^+} of 4.29×10^{-4} S·cm^{-1}, a bigger t_{Li^+} of 0.44 and an enlarged SEWV of 4.8 V vs. Li/Li^+ at 30 °C. Moreover, an exceptional compatibility and stability with an improved CCD of 1.2 mA·cm^{-2} was obtained against lithium dendrites. More importantly, the as-prepared PVDF-LLZTO@12C4-TFSI-5 CPE enables the assembled Li‖$LiFePO_4$ solid-state cell to cycle steadily for over 750 cycles at 1.0 C with a capacity retention of 87.2%. The assembled pouch cell can steadily light LED lamp under variously crucial conditions. This work provides a new insight for optimizing interface impedance of CPE and sheds lights on the development of PVDF-LLZTO CPE based SSLBs.

Electronic Supplementary Material: Supplementary material (additional materials such as ^{1}H NMR spectra, ^{6}Li NMR spectra, FTIR spectra, XRD patterns, XPS spectra, SEM images, digital photographs, Nyquist plots of the cells, and comparison tables) is available in the online version of this article at https://doi.org/10.26599/NR.2025.94907087.

Data availability

All data needed to support the conclusions in the paper are presented in the manuscript and the Electronic Supplementary Material. Additional data related to this paper may be requested from the corresponding author upon request.

Acknowledgements

We gratefully acknowledge the financial support of the National Key Research and Development Program of China (No. 2021YFE0107200), the National Natural Science Foundation of China (No. 21773167), and the Key R&D Project funded by Department of Science and Technology of Jiangsu Province (No. BE2020003).

Declaration of competing interest

All the contributing authors no conflict of interests in this work.

Author contribution statement

C. F. L.: Writing – original draft, methodology, investigation, formal analysis. S. L. W.: Formal analysis, software. Z. Y. L.: Formal analysis, methodology. J. Q. Z.: Drawing. Y. C. W.: Methodology. C. J. R.: Visualization. R. Z. Y.: Resources, project administration. C. J.: Writing – review & editing, supervision, funding acquisition, conceptualization.

Use of AI statement

None.

References

[1] Deng, Q.; Zhang, Q. M.; Chu, Y. Q.; Xu, Y. K.; You, S. Z.; Huang, K.; Yang, C. H.; Lu, J. Understanding improved stability of Co-free Ni-rich single crystal cathode materials by combined bulk and surface modifications. *Mater. Today* **2024**, *74*, 22–33.

[2] Bi, Z. J.; Guo, X. X. Solidification for solid-state lithium batteries with high energy density and long cycle life. *Energy Mater.* **2022**, *2*, 200011.

[3] Zhang, Q. M.; Deng, Q.; Zhong, W. T.; Li, J.; Wang, Z. M.; Dong, P. Y.; Huang, K.; Yang, C. H. Tungsten boride stabilized single-crystal $LiNi_{0.83}Co_{0.07}Mn_{0.1}O_2$ cathode for high energy density lithium-ion batteries: Performance and mechanisms. *Adv. Funct. Mater.* **2023**, *33*, 2301336.

[4] Kong, M. J.; Wu, J. F. Nanometer scale lithium-ion conducting oxides: $Li_{6.1}Ga_{0.3}La_3Zr_2O_{12}$ and $Li_{0.3}La_{0.57}TiO_3$. *Solid State Ionics* **2024**, *414*, 116635.

[5] Zhang, B. K.; Tan, R.; Yang, L. Y.; Zheng, J. X.; Zhang, K. C.; Mo, S. J.; Lin, Z.; Pan, F. Mechanisms and properties of ion-transport in inorganic solid electrolytes. *Energy Storage Mater.* **2018**, *10*, 139–159.

[6] Dai, D. M.; Yang, L. F.; Zheng, S. M.; Niu, J.; Sun, Z.; Wang, B.; Yang, Y. F.; Li, B., Modified alginate dressing with high thermal stability as a new separator for Li-ion batteries. Chem. *Commun.* **2020**, *56*, 6149–6152.

[7] Pei, F.; Wu, L.; Zhang, Y.; Liao, Y. Q.; Kang, Q.; Han, Y.; Zhang, H. W.; Shen, Y.; Xu, H. H.; Li, Z. et al. Interfacial self-healing polymer electrolytes for long-cycle solid-state lithium-sulfur batteries. *Nat. Commun.* **2024**, *15*, 351.

[8] Li, J.; Yang, H.; Deng, Q.; Li, W. M.; Zhang, Q. M.; Zhang, Z. H.; Chu, Y. Q.; Yang, C. H. Stabilizing Ni-rich single-crystalline $LiNi_{0.83}Co_{0.07}Mn_{0.10}O_2$ cathodes using Ce/Gd Co-doped high-entropy composite surfaces. *Angew. Chem., Int. Ed.* **2024**, *63*, e202318042.

[9] Li, B.; Wang, X. B.; Gao, Y. B.; Wang, B.; Qiu, J. X.; Cheng, X.; Dai, D. M. Improving rate performances of Li-rich layered oxide by the codoping of Sn and K ions. *J. Materiomics* **2019**, *5*, 149–155.

[10] Lu, Z. Y.; Peng, L.; Rong, Y.; Wang, E. L.; Shi, R. H.; Yang, H. X.; Xu, Y. D.; Yang, R. Z.; Jin, C. Enhanced electrochemical properties and optimized Li^+ transmission pathways of PEO/LLZTO-based composite electrolytes modified by supramolecular combination. *Energy Environ. Mater.* **2024**, *7*, e12498.

[11] Rong, Y.; Lu, Z. Y.; Jin, C.; Xu, Y. D.; Peng, L.; Shi, R. H.; Gu, T. Y.; Lu, C. Y.; Yang, R. Z. Tailoring of Li/LATP-PEO Interface via a functional organic layer for high-performance solid lithium metal batteries. *ACS Sustain. Chem. Eng.* **2023**, *11*, 785–795.

[12] Lu, Z. Y.; Liu, C. F.; Wang, E. L.; Yang, R. Z.; Yang, H. X.; Jin, C. Two-step strategy to optimize interfacial compatibility of polyether sulfone-$Li_{6.75}La_3Zr_{1.75}Ta_{0.25}O_{12}$ composite polymer electrolytes with Li anode for solid lithium battery with a wide working temperature range. *J. Power Sources* **2024**, *596*, 234101.

[13] Zhang, X.; Liu, T.; Zhang, S. F.; Huang, X.; Xu, B. Q.; Lin, Y. H.; Xu, B.; Li, L. L.; Nan, C. W.; Shen, Y. Synergistic coupling between $Li_{6.75}La_3Zr_{1.75}Ta_{0.25}O_{12}$ and poly(vinylidene fluoride) induces high ionic conductivity, mechanical strength, and thermal stability of solid composite electrolytes. *J. Am. Chem. Soc.* **2017**, *139*, 13779–13785.

[14] Jiang, T. L.; He, P. G.; Wang, G. X.; Shen, Y.; Nan, C. W.; Fan, L. Z. Solvent-free synthesis of thin, flexible, nonflammable garnet-based composite solid electrolyte for all-solid-state lithium batteries. *Adv. Energy Mater.* **2020**, *10*, 1903376.

[15] Dai, D. M.; Zhou, X. X.; Yan, P. Y.; Zhang, Z. Z.; Wang, L.; Wu, C. H.; Li, H. W.; Li, W. T.; Jia, M. M.; Li, B. et al. Interconnected three-dimensional porous alginate-based gel electrolytes for lithium metal batteries. *ACS Appl. Mater. Interfaces* **2024**, *16*, 2428–2437.

[16] Seong, W. M.; Kim, Y.; Manthiram, A. Impact of residual lithium on the adoption of high-nickel layered oxide cathodes for lithium-ion batteries. *Chem. Mater.* **2020**, *32*, 9479–9489.

[17] Li, Y. T.; Chen, X.; Dolocan, A.; Cui, Z. M.; Xin, S.; Xue, L. G.; Xu, H. H.; Park, K.; Goodenough, J. B. Garnet electrolyte with an ultralow interfacial resistance for Li-metal batteries. *J. Am. Chem. Soc.* **2018**, *140*, 6448–6455.

[18] Jeong, W.; Park, S. S.; Yun, J.; Shin, H. R.; Moon, J.; Lee, J. W. Tailoring grain boundary structures and chemistry of $Li_7La_3Zr_2O_{12}$ solid electrolytes for enhanced air stability. *Energy Storage Mater.* **2023**, *54*, 543–552.

[19] Deng, S. W.; Zhu, H. L.; Zheng, Z. Y.; Kong, Z. X.; Wang, Z. X.; Zhou, W.; Tang, R.; Wu, J. F.; Liu, J. L. Synergistically engineering grains and grain boundaries toward Li dendrite-free $Li_7La_3Zr_2O_{12}$. *Nano Lett.* **2024**, *24*, 9801–9807.

[20] Yu, J.; Kwok, S. C. T.; Lu, Z. H.; Effat, M. B.; Lyu, Y. Q.; Yuen, M. M. F.; Ciucci, F. A ceramic-PVDF composite membrane with modified interfaces as an ion-conducting electrolyte for solid-state lithium-ion batteries operating at room temperature. *ChemElectroChem* **2018**, *5*, 2873–2881.

[21] Zhang, Q. M.; Wang, Y. Z.; Deng, Q.; Chu, Y. Q.; Dong, P. Y.; Chen, C. D.; Wang, Z. M.; Xia, Z. G.; Yang, C. H. *In situ* and real-time monitoring the chemical and thermal evolution of lithium-ion batteries with single-crystalline Ni-rich layered oxide cathode. *Angew. Chem., Int. Ed.* **2024**, *63*, e202401716.

[22] Kuhnert, E.; Ladenstein, L.; Jodlbauer, A.; Slugovc, C.; Trimmel, G.; Wilkening, H. M. R.; Rettenwander, D. Lowering the interfacial resistance in $Li_{6.4}La_3Zr_{1.4}Ta_{0.6}O_{12}$. poly(ethylene oxide) composite electrolytes. *Cell Rep. Phys. Sci.* **2020**, *1*, 100214.

[23] Wu, Y. C.; Chao, M.; Lu, C. Y.; Xu, H. Y.; Zeng, K.; Li, D. C.; Yang, R. Z. Surface-functionalized $Li_{1.3}Al_{0.3}Ti_{1.7}(PO_4)_3$ with synergetic silane coupling agent and ionic liquid modification for PEO-based all-solid-state lithium metal batteries. *J. Power Sources* **2024**, *599*, 234206.

[24] Zhao, L.; Yu, X. N.; Jiao, J. Y.; Song, X.; Cheng, X.; Liu, M.; Wang, L. L.; Zheng, J. X.; Lv, W.; Zhong, G. M. et al. Building cross-phase ion transport channels between ceramic and polymer for highly conductive composite solid-state electrolyte. *Cell Rep. Phys. Sci.* **2023**, *4*, 101382.

[25] Peng, L.; Lu, Z. Y.; Zhong, L.; Jian, J. J.; Rong, Y.; Yang, R. Z.; Xu, Y. D.; Jin, C. Enhanced ionic conductivity and interface compatibility of PVDF-LLZTO composite solid electrolytes by interfacial maleic acid modification. *J. Colloid Interface Sci.* **2022**, *613*, 368–375.

[26] Tong, R. A.; Chen, L. H.; Shao, G.; Wang, H. L.; Wang, C. A. An integrated solvent-free modification and composite process of $Li_{6.4}La_3Zr_{1.4}Ta_{0.6}O_{12}$/poly(ethylene oxide) solid electrolytes: Enhanced compatibility and cycle performance. *J. Power Sources* **2021**, *492*, 229672.

[27] Wang, Y.; Chen, Z.; Wu, Y. X.; Li, Y.; Yue, Z. Y.; Chen, M. H. PVDF-HFP/PAN/PDA@LLZTO composite solid electrolyte enabling reinforced safety and outstanding low-temperature performance for quasi-solid-state lithium metal batteries. *ACS Appl. Mater. Interfaces* **2023**, *15*, 21526–21536.

[28] Lu, Z. Y.; Guo, Y.; Zhang, S. W.; Wu, S. C.; Meng, R. W.; Hong, S.; Li, J. X.; Xue, H. Y.; Zhang, B. Y.; Fan, D. H. et al. Crowning metal ions by supramolecularization as a general remedy toward a dendrite-free alkali-metal battery. *Adv. Mater.* **2021**, *33*, 2101745.

[29] Dillon, R. E. A.; Shriver, D. F. Ion transport in cryptand and crown ether lithium salt complexes. *Chem. Mater.* **1999**, *11*, 3296–3301.

[30] Chen, J.; Deng, X. T.; Gao, Y. Y.; Zhao, Y. J.; Kong, X. P.; Rong, Q.; Xiong, J. Q.; Yu, D. M.; Ding, S. J. Multiple dynamic bonds-driven integrated cathode/polymer electrolyte for stable all-solid-state lithium metal batteries. *Angew. Chem., Int. Ed.* **2023**, *62*, e202307255.

[31] Han, Q. Y.; Wang, S. Q.; Jiang, Z. Y.; Hu, X. C.; Wang, H. H. Composite polymer electrolyte incorporating metal-organic framework nanosheets with improved electrochemical stability for all-solid-state Li metal batteries. *ACS Appl. Mater. Interfaces* **2020**, *12*, 20514–20521.

[32] Shen, Y.; Deng, K. M.; Chen, Q. H.; Gao, G.; Li, L. Crowning lithium ions in hole-transport layer toward stable perovskite solar cells. *Adv. Mater.* **2022**, *34*, 2200978.

[33] Yusim, Y.; Moryson, Y.; Seipp, K.; Sann, J.; Henss, A. Challenges in XPS analysis of PEO-LiTFSI-based solid electrolytes: How to overcome X-ray-induced photodecomposition. *Batter. Supercaps* **2024**, *7*, e202400161.

[34] Whba, R.; Su'ait, M. S.; TianKhoon, L.; Ibrahim, S.; Mohamed, N. S.; Ahmad, A. *In-situ* UV cured acrylonitrile grafted epoxidized natural rubber (ACN-*g*-ENR)-LiTFSI solid polymer electrolytes for lithium-ion rechargeable batteries. *React. Funct. Polym.* **2021**, *164*, 104938.

[35] Yu, C. H.; Cho, C. S.; Li, C. C. Well-dispersed garnet crystallites for applications in solid-state Li-S batteries. *ACS Appl. Mater. Interfaces* **2021**, *13*, 11995–12005.

[36] Sun, Y.; Zhan, X. W.; Hu, J. Z.; Wang, Y. K.; Gao, S.; Shen, Y. H.; Cheng, Y. T. Improving ionic conductivity with bimodal-sized $Li_7La_3Zr_2O_{12}$ fillers for composite polymer electrolytes. *ACS Appl. Mater. Interfaces* **2019**, *11*, 12467–12475.

[37] Zhang, S. S.; Li, Z.; Guo, Y.; Cai, L. R.; Manikandan, P.; Zhao, K. J.; Li, Y.; Pol, V. G. Room-temperature, high-voltage solid-state lithium battery with composite solid polymer electrolyte with *in-situ* thermal safety study. *Chem. Eng. J.* **2020**, *400*, 125996.

[38] Xu, Y. N.; Wang, K.; Zhang, X. D.; Ma, Y. B.; Peng, Q. F.; Gong, Y.; Yi, S.; Guo, H.; Zhang, X.; Sun, X. Z. et al. Improved Li-ion conduction and (electro)chemical stability at garnet-polymer interface through metal-nitrogen bonding. *Adv. Energy Mater.* **2023**, *13*, 2204377.

[39] Fan, K. B.; Lai, X. X.; Zhang, Z. Q.; Chai, L. L.; Yang, Q. C.; He, G. H.; Liu, S.; Sun, L.; Zhao, Y.; Hu, Z. G. et al. Poly(vinylidene fluoride)-based dual-salt composite polymer electrolytes for superior room-temperature solid-state lithium batteries. *J. Power Sources* **2023**, *580*, 233342.

[40] Luo, B.; Wu, J. T.; Zhang, M.; Zhang, Z. H.; Zhang, X. W.; Fang, Z. X.; Xu, Z. Q.; Wu, M. Q. Surface modification of garnet fillers with a polymeric sacrificial agent enables compatible interfaces of composite solid-state electrolytes. *Chem. Sci.* **2023**, *14*, 13067–13079.

[41] Hu, J. K.; He, P. G.; Zhang, B. C.; Wang, B. Y.; Fan, L. Z. Porous film host-derived 3D composite polymer electrolyte for high-voltage solid state lithium batteries. *Energy Storage Mater.* **2020**, *26*, 283–289.

[42] Lu, J.; Liu, Y. C.; Yao, P. H.; Ding, Z. Y.; Tang, Q. M.; Wu, J. W.; Ye, Z. R.; Huang, K.; Liu, X. J. Hybridizing poly(vinylidene fluoride-co-hexafluoropropylene) with $Li_{6.5}La_3Zr_{1.5}Ta_{0.5}O_{12}$ as a lithium-ion electrolyte for solid state lithium metal batteries. *Chem. Eng. J.* **2019**, *367*, 230–238.

[43] Zhang, W. Q.; Nie, J. H.; Li, F.; Wang, Z. L.; Sun, C. W. A durable and safe solid-state lithium battery with a hybrid electrolyte membrane. *Nano Energy* **2018**, *45*, 413–419.

[44] Duan, T.; Cheng, H. W.; Sun, Q. C.; Liu, Y. B.; Nie, W.; Chu, Y. H.; Xu, Q.; Lu, X. G. Reinforcing interfacial compatibility of LLZTO/PVDF-HFP composite electrolytes by chemical interaction for solid-state lithium metal batteries. *J. Power Sources* **2024**, *589*, 233789.

[45] Zhang, S. Q. Suppressing Li dendrites via electrolyte engineering by crown ethers for lithium metal batteries. *Nano-Micro Lett.* **2020**, *12*, 158.

[46] Zeng, F. Y.; Sun, Y. Y.; Hui, B.; Xia, Y. Z.; Zou, Y. H.; Zhang, X. L.; Yang, D. J. Three-dimensional porous alginate fiber membrane

reinforced PEO-based solid polymer electrolyte for safe and high-performance lithium ion batteries. *ACS Appl. Mater. Interfaces* **2020**, *12*, 43805–43812.

[47] Wu, M. J.; Song, J. P.; Lei, J. H.; Tang, H. L. An artificial interphase enables stable PVDF-based solid-state Li metal batteries. *Nano Res.* **2024**, *17*, 1482–1490.

[48] Li, W. W.; Sun, C. Z.; Jin, J.; Li, Y. P.; Chen, C. H.; Wen, Z. Y. Realization of the Li^+ domain diffusion effect via constructing molecular brushes on the LLZTO surface and its application in all-solid-state lithium batteries. *J. Mater. Chem. A* **2019**, *7*, 27304–27312.

[49] Zhou, J. Ionic conductivity of composite electrolytes based on oligo(ethylene oxide) and fumed oxides. *Solid State Ionics* **2004**, *166*, 275–293.

[50] Zhang, Q. M.; Chu, Y. Q.; Wu, J. X.; Dong, P. Y.; Deng, Q.; Chen, C. D.; Huang, K.; Yang, C. H.; Lu, J. Mitigating planar gliding in single-crystal nickel-rich cathodes through multifunctional composite surface engineering. *Adv. Energy Mater.* **2024**, *14*, 2303764.

[51] Juan, J.; Fernández-Werner, L.; Jasen, P. V.; Bechthold, P.; Faccio, R.; González, E. A. Theoretical study of Li intercalation in TiO_2(B) surfaces. *Appl. Surf. Sci.* **2020**, *526*, 146460.

[52] Guo, Q.; Cheng, X. P.; Shi, Y. W.; Sheng, Z. M.; Chang, C. K. Bluish $Li_4Ti_5O_{12}$ with enhanced rate performance. *J. Alloys Compd.* **2017**, *710*, 383–392.

[53] Yang, B. B.; Deng, C. L.; Chen, N.; Zhang, F. L.; Hu, K. K.; Gui, B. S.; Zhao, L. Y.; Wu, F.; Chen, R. J. Super-ionic conductor soft filler promotes Li^+ transport in integrated cathode-electrolyte for solid-state battery at room temperature. *Adv. Mater.* **2024**, *36*, 2403078.

[54] Guan, S. D.; Wen, K. H.; Liang, Y.; Xue, C. J.; Liu, S. J.; Yu, J. Y.; Zhang, Z.; Wu, X. B.; Yuan, H. V.; Lin, Z. Y. et al. An organic additive assisting with high ionic conduction and dendrite resistance of polymer electrolytes. *J. Mater. Chem. A* **2022**, *10*, 24269–24279.

[55] Pei, R. J.; Song, T. Y.; Sun, L. L.; Li, Y. F.; Yang, R. Stable composite electrolytes of PVDF modified by inorganic particles for solid-state lithium batteries. *J. Am. Ceram. Soc.* **2022**, *105*, 5262–5273.

[56] Yeh, S. M.; Li, C. C. Enhancing Li^+ transport efficiency in solid-state Li-ion batteries with a ceramic-array-based composite electrolyte. *J. Mater. Chem. A* **2023**, *11*, 24390–24402.

[57] Pan, X. W.; Sun, J. W.; Jin, C.; Wang, Z. J.; Xiao, R. J.; Peng, L.; Shen, L. W.; Li, C.; Yang, R. Z. A flexible composite electrolyte membrane with ultrahigh LLZTO garnet content for quasi solid state Li-air batteries. *Solid State Ionics* **2020**, *351*, 115340.

[58] Fritsch, C.; Zinkevich, T.; Indris, S.; Etter, M.; Baran, V.; Bergfeldt, T.; Knapp, M.; Ehrenberg, H.; Hansen, A. L. Garnet to hydrogarnet: Effect of post synthesis treatment on cation substituted LLZO solid electrolyte and its effect on Li ion conductivity. *RSC Adv.* **2021**, *11*, 30283–30294.

[59] Buschmann, H.; Dölle, J.; Berendts, S.; Kuhn, A.; Bottke, P.; Wilkening, M.; Heitjans, P.; Senyshyn, A.; Ehrenberg, H.; Lotnyk, A. et al. Structure and dynamics of the fast lithium ion conductor "$Li_7La_3Zr_2O_{12}$". *Phys. Chem. Chem. Phys.* **2011**, *13*, 19378–19392.

[60] van Wüllen, L.; Echelmeyer, T.; Meyer, H. W.; Wilmer, D. The mechanism of Li-ion transport in the garnet $Li_5La_3Nb_2O_{12}$. *Phys. Chem. Chem. Phys.* **2007**, *9*, 3298–3303.

[61] Wang, D. W.; Zhong, G. M.; Pang, W. K.; Guo, Z. P.; Li, Y. X.; McDonald, M. J.; Fu, R. Q.; Mi, J. X.; Yang, Y. Toward understanding the lithium transport mechanism in garnet-type solid electrolytes: Li^+ ion exchanges and their mobility at octahedral/tetrahedral sites. *Chem. Mater.* **2015**, *27*, 6650–6659.

This is an open access article under the terms of the Creative Commons Attribution 4.0 International License (CC BY 4.0, https://creativecommons.org/licenses/by/4.0/).

© The Author(s) 2025. Published by Tsinghua University Press.